NANO · MICRO small
www.small-journal.com

Highly Conductive Networks of Silver Nanosheets

*Adam G. Kelly, Jane O'Reilly, Cian Gabbett, Beata Szydłowska, Domhnall O'Suilleabhain, Umar Khan, Jack Maughan, Tian Carey, Siadhbh Sheil, Plamen Stamenov, and Jonathan N. Coleman**

Although printed networks of semiconducting nanosheets have found success in a range of applications, conductive nanosheet networks are limited by low conductivities (<10^6 S m^{-1}). Here, dispersions of silver nanosheets (AgNS) that can be printed into highly conductive networks are described. Using a commercial thermal inkjet printer, AgNS patterns with unannealed conductivities of up to (6.0 ± 1.1) × 10^6 S m^{-1} are printed. These networks can form electromagnetic interference shields with record shielding effectiveness of >60 dB in the microwave region at thicknesses <200 nm. High resolution patterns with line widths down to 10 µm are also printed using an aerosol-jet printer which, when annealed at 200 °C, display conductivity >10^7 S m^{-1}. Unlike conventional Ag-nanoparticle inks, the 2D geometry of AgNS yields smooth, short-free interfaces between electrode and active layer when used as the top electrode in vertical nanosheet heterostructures. This shows that all-printed vertical heterostructures of AgNS/WS_2/AgNS, where the top electrode is a mesh grid, function as photodetectors demonstrating that such structures can be used in optoelectronic applications that usually require transparent conductors.

1. Introduction

Over the past decade, a wide range of solution-processed semiconducting 2D nanosheets have been used as active materials in various printed electronic devices.[1–3] The complexity of these devices has evolved from simple capacitors and photodetectors[4] to photovoltaics[5] and thin-film transistors.[6,7] However, the incorporation of conducting nanosheets into such devices (e.g., as-printed electrodes) has been hindered by the limited availability of conductive nanosheets, with only graphene-[8,9] or MXene-based inks available.[10,11] While graphene networks can display conductivities >10^5 S m^{-1},[12] state-of-the-art printed graphene networks are <10^5 S m^{-1} with the uppermost values only achieved via high temperature annealing[8,13] or compression,[14] or both.[15] Inkjet-printable MXenes have demonstrated conductivities >10^5 S m^{-1},[10,11], but the maximum reported value is currently ≈10^6 S m^{-1}.[16] The conductivities of these networks are usually limited by inter-sheet junction resistances[1,17] and are well below the typical values of 3–6 × 10^7 S m^{-1} displayed by metals such as silver, gold, and copper. Conductive polymers such as poly(3,4-ethylenedioxythiophene) polystyrene sulfonate (PEDOT:PSS) can also reach conductivities >10^5 S m^{-1}, but these values are reached using acidic post-treatments and as-printed values are orders of magnitude lower.[18]

This is a significant gap as highly conductive networks are important for printed electrodes,[19] transparent conductors[20,21] and electromagnetic shields.[10,16] For example, silver nanoparticle (AgNP) inks have been commercialized[22] due to their printability and capacity to yield high-conductivity films which typically reach ≈3 × 10^7 S m^{-1} following high temperature (>200 °C) annealing.[23] Inks based on the in situ reduction of silver complexes can lower the processing temperature to ≈100 °C[24,25] however post-treatment is usually still needed to maximize the conductivity.[25,26] Similarly, particle-free reactive silver inks have shown high conductivity (>10^6 S m^{-1}) when processed at room temperature,[27] however the solution-based nature of these inks may preclude them from use in porous heterostructures due to solute penetration into the lower layers. Alternatively, networks of silver nanowires (AgNW) have been used in a range of device applications[28] and when printed, display conductivities up to 10^6 S m^{-1}[29,30] but plasma welding or sintering at over 200 °C[31] is typically required to maximize the network conductivity.

The purpose of sintering/annealing is to minimize the interparticle junction resistances, which is critical for AgNP- or AgNW-based networks due to the low-area, point-like nature of the junctions. A potential low temperature alternative would be

A. G. Kelly, J. O'Reilly, C. Gabbett, B. Szydłowska, D. O'Suilleabhain, J. Maughan, T. Carey, S. Sheil, P. Stamenov, J. N. Coleman
School of Physics
CRANN and AMBER Research Centers
Trinity College Dublin
Dublin 2 D02 W085, Ireland
E-mail: colemaj@tcd.ie

U. Khan
Department of Life Science
School of Science
Institute of Technology Sligo
Ash Lane, Sligo F91 YW50, Ireland

The ORCID identification number(s) for the author(s) of this article can be found under https://doi.org/10.1002/smll.202105996.

© 2022 The Authors. Small published by Wiley-VCH GmbH. This is an open access article under the terms of the Creative Commons Attribution License, which permits use, distribution and reproduction in any medium, provided the original work is properly cited.

DOI: 10.1002/smll.202105996

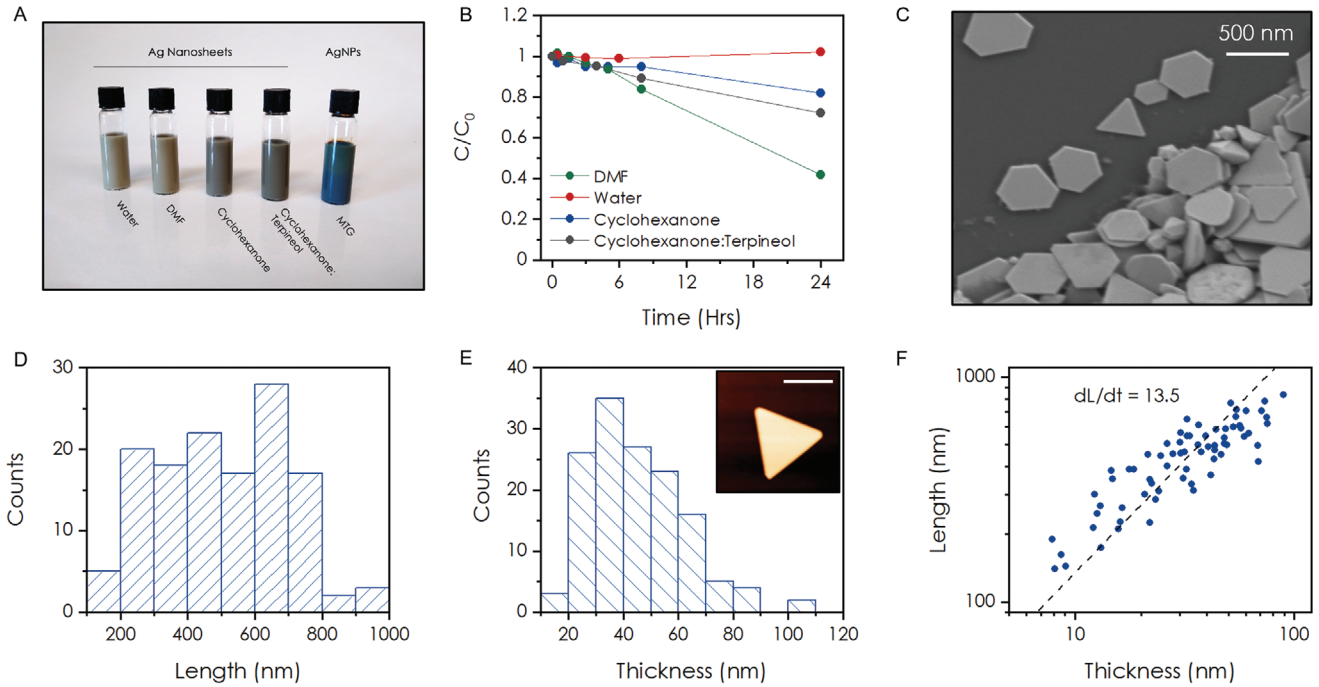

Figure 1. Silver nanosheet characterization. A) An image of silver nanosheets dispersed in a range of solvents. B) The stability the AgNS in various solvents over a 24 h period. Initial concentrations varied between 7–10 mg mL^{-1}. C) An SEM image showing the range of silver nanosheet morphologies from the stock dispersion. D–F) AFM data showing the AgNS length distribution with $<L_{NS}>$ ≈500 nm (D), an asymmetric thickness distribution with $<t_{NS}>$ ≈44 nm (E), and the approximate proportionality between length and thickness. Inset in (E): a representative AFM image of an AgNS. Scale bar = 300 nm.

to use 2D analogues of AgNP or AgNW allowing the formation of large-area inter-particle junctions. This would reduce junction resistance, resulting in efficient inter-sheet charge transfer effecting a high network conductivity.[3] In addition, networks of such materials would combine the conductivity of a film of metal particles with the morphology of a nanosheet network allowing effective interfacing between nanosheet-based active layers in printed devices. While a very few reports already exist on the synthesis[32,32] and deposition[34] of 2D-like silver nanosheets (AgNS), very little is known about AgNS networks and their properties.

Here, we report AgNS as a highly conductive printable material that can be processed at room temperature, which we attribute to the 2D-like aspect ratio. We show that additive-free water-based inks containing AgNS can be printed to form networks with conductivity approaching 10^7 S m^{-1} at ambient processing temperatures and >10^7 S m^{-1} when annealed at 200 °C. Thin AgNS networks (<200 nm thick) shield electromagnetic waves in the microwave-to-visible region with an effectiveness >60 dB. We further demonstrate that the 2D geometry is critical for forming smooth and continuous interfaces in vertical heterostacks as the small diameter of AgNP allows them to penetrate the device which can cause shorting. This allows us to print photodetectors based on AgNS/WS_2/AgNS vertical heterostructures.

2. Results and Discussion

AgNS can be sourced commercially as a highly concentrated (≈94 wt%) water-based paste. Once this paste is diluted to a workable concentration of ≈70 mg mL^{-1}, the AgNS can easily be solvent-exchanged by centrifugation into other common printing solvents such as triethylene glycol monomethyl ether (MTG), DMF, or cyclohexanone as shown in **Figure 1**A (for methods and materials, see Supporting Information S1). Thermogravimetric analysis reveals that ≈1.3 wt% of the solids mass is composed of an organic additive, which allows us to estimate a nanosheet coverage of ≈3 nm per nanosheet (Supporting Information S2). Figure 1B shows the stability of the AgNS in various solvents over 24 h. We see sufficient stability in water, cyclohexanone, and a 90:10 blend of cyclohexanone/terpineol for printing the AgNS without adulterating the dispersion with additional stabilizers such as polymers or surfactants which can negatively affect the electrical properties. As shown in Figure 1C–E, the AgNS are polydisperse with an average length between 250 and 500 nm (Figure 1D), with an average thickness of ≈44 nm (Figure 1E). Figure 1F shows a roughly linear scaling between length and thickness with a characteristic aspect ratio, $k = <L_{NS}/t_{NS}>$, of ≈13.5. Importantly, the basal planes (known to be <111>)[32] of the nanosheets are smooth and continuous (Figure 1E, inset) which should facilitate good inter-sheet contact.

We demonstrated the printability of water-based AgNS using a Canon MG2550 thermal inkjet printer (TIP) to print a large-area image of the Trinity College campanile, shown in **Figure 2**A. This type of commercial printer is optimized for water-based ink deposition and has a nozzle diameter of ≈10 µm (Supporting Information S3). Figure 2B shows a top-down SEM image of an unannealed printed network, where the distortion of the AgNS shapes (the rounding of the typical <111> facets) is

© 2022 The Authors. Small published by Wiley-VCH GmbH

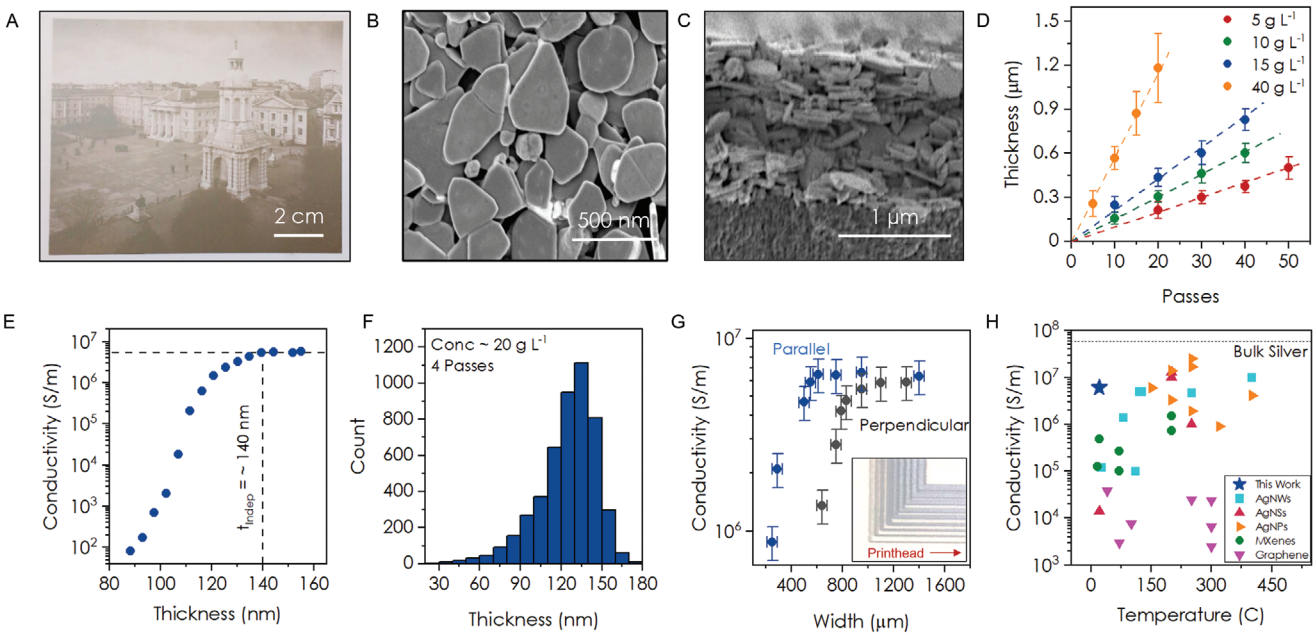

Figure 2. Thermal inkjet printing. A) A printed image of the campanile in Trinity College using 5 print passes where the substrate was held for 5 min following each pass. Adapted with permission, Trinity College Dublin. B) An SEM image of a printed network of AgNS. Some distortion in the edge definition of the nanosheets is visible due to the high temperatures experienced within the printhead. C) A cross-section of the network shown in (B). D) The scaling of the network thickness with number of printing passes for a range of AgNS concentrations. E) The thickness dependence of the conductivity showing a thickness-independent value is reached at >140 nm. F) A thickness histogram obtained using a transmission scanner where each pixel is converted into a thickness value as outlined in Supporting Information S1 and S3. G) The linewidth dependence of the conductivity for lines printed parallel and perpendicular to the direction of the printhead motion. A higher resolution is achievable for lines printed parallel to the motion of the printhead. Inset: lines printed at right angles to each other showing the anisotropic resolution of the printer. H) A comparison of reported conductivities obtained at various post-processing temperatures using various nanomaterials with bulk silver shown for comparison (see Supporting Information).

attributed to the high temperatures reached inside the thermal printhead.[35] Such rounding is accompanied by enhanced SEM charging contrast which may be associated with oxidation at the edges of the AgNS, although more experiments would be required to prove this conclusively. However, we note that the blackening and nanoparticle formation that usually accompany the oxidation of Ag nanowires is not observed here.[36] In any cases, no contrast enhancement is observed on the surface of the platelets suggesting them to be unchanged by the printing process. This is supported by data below which shows the inter-platelet junction resistance to be extremely low.

A cross-section shows the network to be a tightly bound stack where the AgNS show some in-plane alignment (Figure 2C). Although we accept that a single measurement on such a small area cannot provide a statistically meaningful measurement, Figure 2C can be used to give a rough estimate of the network porosity. In Supporting Information S4, we show that image analysis suggests the porosity of printed AgNS networks to be $P = 30 \pm 5\%$, significantly below typical nanosheet networks which display $P \approx 50\%$.[6]

Using such cross-sections, we can find the network thickness per print pass (Figure 2D) which then allows thickness control (see Supporting Information S5). The conductivity of such unannealed networks shows a percolation-type increase[20] with network thickness (t) before reaching a thickness-independent conductivity of $(6.0 \pm 1.1) \times 10^6$ S m^{-1} at $t \approx 140$ nm shown in Figure 2E. This conductivity falls <2% following 13 weeks storage in ambient before falling to 3–4 × 10^6 S m^{-1} after approximately a year (Supporting Information S6). To determine whether the temperature in the printhead affects the conductivity, we also dropcast (Figure 1C) and spray-coat (Supporting Information S7) AgNS networks at room temperature where we measure a conductivity of $(6.6 \pm 2.1) \times 10^6$ and $(5.6 \pm 0.9) \times 10^6$ S m^{-1}, respectively. The thickness distribution of a typical network (measured over a 4 × 1 cm area using a transmission scanner[29]) is shown in Figure 2F, with line profiles for various thicknesses shown in Supporting Information S8. Although the network shows a relatively low $\Delta t/\langle t \rangle$ ratio of 17%, the thickness distribution is somewhat asymmetric with some regions displaying local thicknesses as low as ≈32% of $\langle t \rangle$. The resolution limits of the printer become clear as the conductivity falls off for linewidths <400 µm due to line edge roughness (Figure 2G). Furthermore, the dependence of conductivity on linewidth is sensitive to the printing direction relative to the printhead motion (Figure 2G, inset) with lines printed parallel to the direction of travel more uniform than those printed perpendicular.

A comparison between conductivity and processing temperature across various nanoscale electrical conductors shown in Figure 2H (see Supporting Information T1). High conductivities achieved at low processing temperatures appear in the upper left quadrant. While room-temperature processing of AgNW[37] and AgNS[38] has been reported, the conductivity of the TIJ-printed AgNS outperforms other silver nanomaterials at low temperature and outperforms all other 2D systems at all processing temperatures as would be expected for a 2D metal.

© 2022 The Authors. Small published by Wiley-VCH GmbH

This maximum observed conductivity of ≈6 × 10^6 S m^{-1} is approximately ten times lower than bulk crystalline silver but close to bulk manganese (7 × 10^6 S m^{-1}). As these networks appear to have low porosity (P ≈ 30%), we attribute this difference mainly to the effects of inter-sheet junction resistance.[1] A key advantage of 2D materials over other nanoscale geometries is their large basal planes which can create large-area junctions between the nanosheets, potentially leading to low junction resistance.[3,39] We can estimate the junction resistance, R_J, from the network conductivity[1] using $\sigma_{Net} \approx (1 - P)/t_{NS}R_J$ and the measured value of $P = 0.3$, yielding R_J ≈3 Ω. We can compare this to the estimated nanosheet resistance via $R_{NS} \approx (t_{NS}\sigma_{Ag})^{-1}$,[1] obtaining R_{NS} ≈0.4 Ω confirming these networks to be junction limited. This compares to R_J of ≈10-25 Ω for post-processed AgNW networks,[40] and R_J ≈10^2–10^6 Ω for graphene and MXene networks.[1]

The estimated junction resistance for AgNS is clearly much closer to that of AgNW networks than van der Waals bonded systems such as graphene. This indicates that the junctions are metallic in nature. We suggest that these low resistance junctions may be due to the formation of silver filaments in the junction region which locally displace the organics coating the nanosheets and form robust electrical connections between nanosheets. In AgNW networks, such connections have been formed via electromigration-induced filament formation, which can be instigated either optically or thermally.[41,42] It is likely that the junction resistance associated with inter-AgNS junctions is smaller than that associated with inter-AgNW junctions simply because the 2D nature of the former leads to greater overlap area and scope for larger area inter-sheet, metallic connections. Here, the robustness of the inter-sheet connections is evidenced by their stability when exposed to ultrasonic agitation in isopropanol and acetone for tens of minutes (Supporting Information S9). In addition, this relatively low junction resistance highlights the benefits of the 2D geometry demonstrating the advantage of AgNS networks.

Highly conductive networks have many applications. For example, electromagnetic interference (EMI) shielding is increasingly important in the electronics industry, with typical applications requiring a shielding effectiveness of >20 dB (99% shielding)[43] at minimal coating thickness. The total shielding effectiveness, EMI SE, has two components representing reflection and absorption and is described previously:[44]

$$\text{EMI SE} = 10\log\left(\frac{\sigma}{100 f\varepsilon_0}\right) + 8.69t\sqrt{\pi f\mu_0\sigma} \quad (1)$$

where σ is the conductivity in S m^{-1}, f is the frequency in Hz, and t is the thickness in m (see Supporting Information S10 for further discussion). Printed AgNS networks are potentially very promising EMI shields due to their high conductivity.

Figure 3A shows an optical image of conductive traces composed of printed AgNS networks of various thicknesses. Figure 3B shows the EMI SE for a range of network thicknesses measured in the X band. While networks below t ≈80 nm show no shielding beyond the substrate, the EMI SE for both the X-K_U and K bands rapidly increase once σ_{Net} surpasses ≈100 S m^{-1}. While thinner films show some absorption, the networks become fully reflective in the X-K_U band once the conductivity saturates (Supporting Information S11). Multi-band shielding is also demonstrated for the K and K_a bands and optical wavelengths in Supporting Information S11 and S12 where the transition from transmissive to shielding behavior also occurs in the region where the AgNS network becomes conductive.

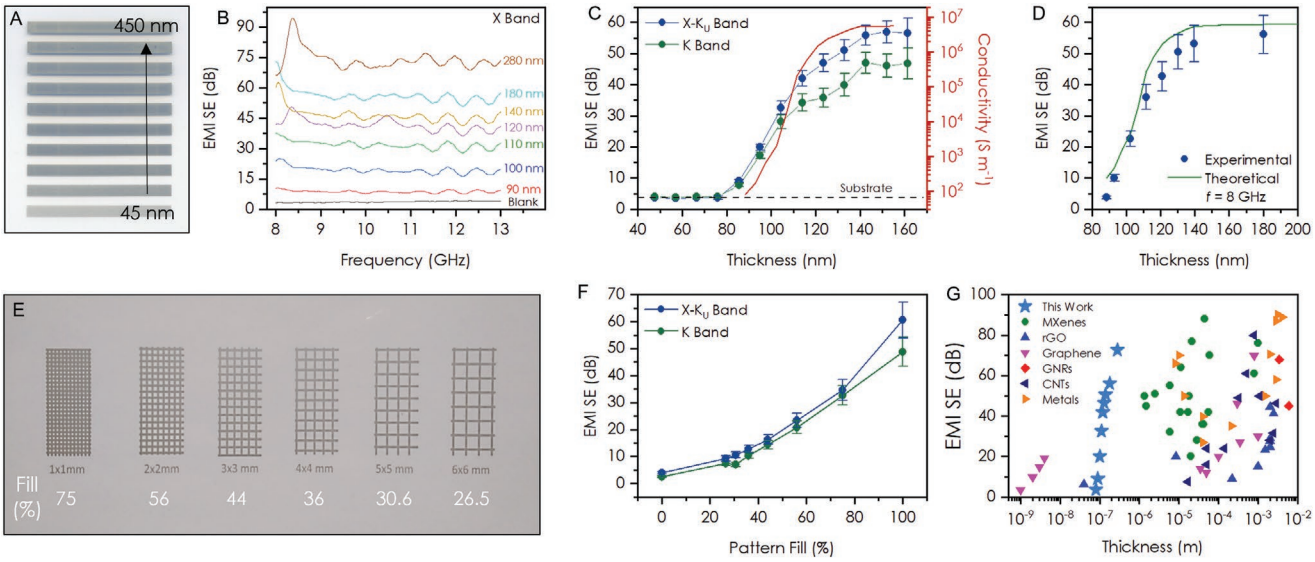

Figure 3. EMI Shields created from inkjet-printed networks. A) An optical image of networks printed with a 30 mg mL^{-1} ink of various thicknesses achieved by printing for 1–10 passes. B) Total shielding effectiveness across the X band for a range of film thicknesses. C) Percolation-like scaling of the shielding effectiveness with film thickness for the X-K_U and K bands. The conductivity data from Figure 2 E is replotted for comparison. D) A comparison of experimentally measured EMI SE across a range of thicknesses with calculated values using the conductivity data from Figure 2E with Equation (1). E) An optical image showing various grids printed with varied apertures. F) The total shielding effectiveness as a function of grid fill factor for the X-K_U and K bands. G) The total shielding effectiveness against thickness for a range of nanomaterials and metals (see Supporting Information T2 for details). The star symbols represent AgNS networks.

© 2022 The Authors. Small published by Wiley-VCH GmbH

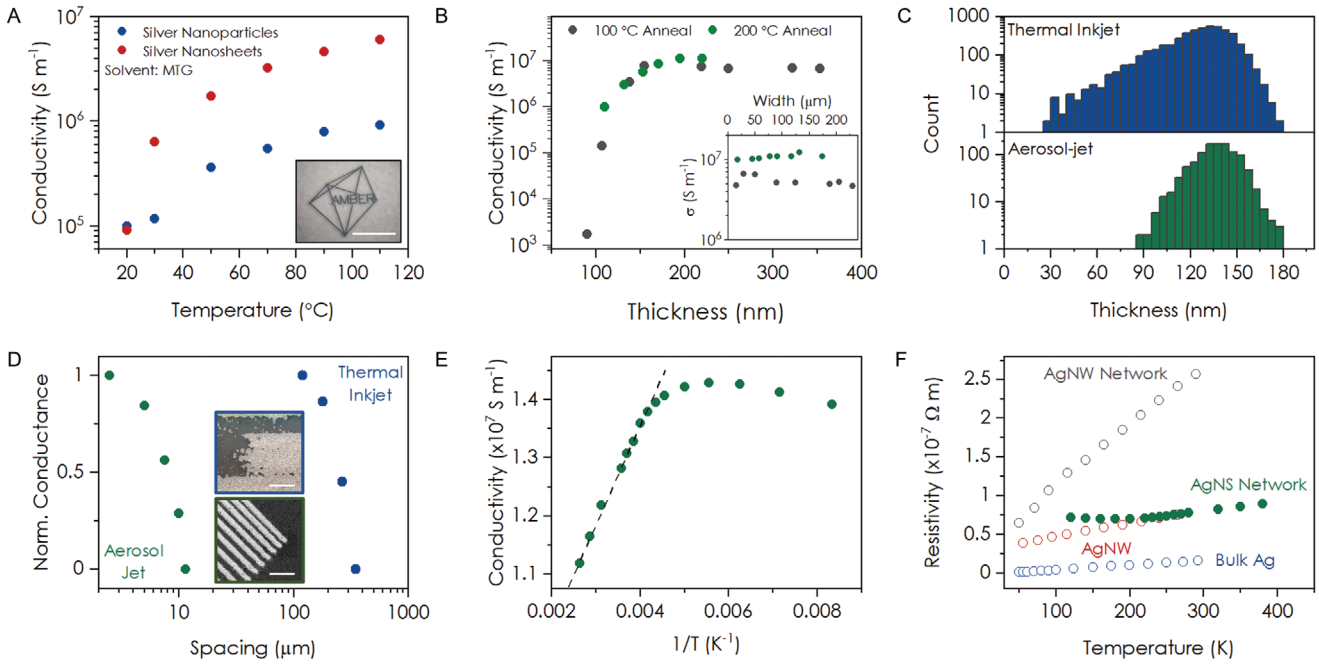

Figure 4. Aerosol-jet printed AgNS characterization. A) Conductivity versus annealing temperature for AgNS and commercial Ag-nanoparticle inks, both printed on PET using triethylene glycol monomethyl ether (MTG) solvent. Inset: the AMBER logo printed on PET. Scale bar: 250 μm. B) The thickness dependence of the conductivity for both PET and glass substrates. The PET sample is annealed at 100 °C and the glass sample is annealed at 200 °C. Inset: the width dependence of the conductivity for samples printed on PET (grey) and glass (green) substrates. C) Histograms comparing the thickness distribution of networks with similar average thickness deposited by thermal inkjet and aerosol-jet printing. D) The onset of crosstalk between closely spaced lines for aerosol-jet printed lines and thermal inkjet-printed lines. The conduction between the lines is zero where the resistance goes to infinity (or conductance goes to zero). Inset (blue): an optical image of thermal inkjet printed lines with evident line edge roughness. Scale bar: 500 μm. Inset (green): an SEM image of closely spaced aerosol-jet printed lines. Scale bar: 50 μm. E) The conductivity of the C:T ink as a function of temperature. The AgNS network shows a metal–insulator transition at ≈180 K, with typical metallic behavior seen at $T > 240$ K indicated by the dashed line which is a guide for the eye. F) The resistivity of the AgNS network plotted as a function of temperature with data reproduced under the terms of the Creative Commons Attribution 4.0 International License.[46] (Copyright 2015, The Author(s), Published by Springer Nature) for an individual AgNW and bulk silver (Reproduced with permission.[47] Copyright 2016, Royal Society of Chemistry) for an AgNW network shown for comparison.

Using the thickness and conductivity data from Figure 2E combined with Equation (1), we find good agreement with the predicted EMI SE in the range of thicknesses above $t \approx 80$ nm as shown in Figure 3D and Supporting Information S13.

It is also desirable to create EMI shields that combine optical transparency with microwave shielding, often achieved using a mesh grid,[45] a design easily produced via printing. A series of printed mesh grids is shown in Figure 3E where the linewidth and network thickness are kept constant at 1 and 300 nm, respectively. The aperture length, D, is varied from 1 to 6 mm which corresponds to reduction in material fill factor (compared to a complete film) from 75% to 26.5%. As shown in Figure 3F, we observe over 99.9% shielding efficiency (30 dB) at a 75% fill and 99% shielding efficiency (20 dB) at a 56% fill for both the X-K_U and K bands. Similar behavior is seen across multiple frequency bands with a suppressed effect at higher frequencies caused by the deeper penetration into the network (Supporting Information S14). While many nanomaterials have demonstrated significant EMI SE at low thickness, the AgNS presented in this work outperform the reported materials to date with EMI SE values of >60 dB reached for thicknesses of 180 nm as shown in Figure 3G (see Supporting Information T2 for details). Despite the high density of silver, the AgNS networks also outperform all other materials when comparing the thickness-normalized specific shielding effectiveness (see Supporting Information S15).

The AgNS are also compatible with more sophisticated deposition techniques such as aerosol-jet printing (AJP) where far higher resolutions than commercial TIJ are achievable[46] and some of the TIJ-induced degradation of the AgNS can be avoided. For example, **Figure 4**A, inset, shows the AMBER center logo printed on PET using MTG-based AgNS ink show linewidths <15 μm wide. To compare the conductivity of AgNS and AgNP networks, we dispersed both in MTG, a solvent commonly used in commercial AgNP inks, and printed conductive traces which were annealed at a range of temperatures below 120 °C. At room temperature, the AgNS and AgNP show a similarly low conductivity which we attribute to the residual MTG in the network owing to its higher boiling point compared to water. This also leads to a comparatively lower room-temperature conductivity than the inkjet-printed AgNS. However, for annealing temperatures above 30 °C the AgNS traces were roughly 10× more conductive than the AgNP (Figure 4A). This again supports the idea that the 2D-like morphology of the AgNS results in lower junction resistances compared to other nanoscale geometries.

While MTG- and water-based inks are suitable for printing on PET, we found 90:10 blend of cyclohexanone:terpineol (C:T)

© 2022 The Authors. Small published by Wiley-VCH GmbH

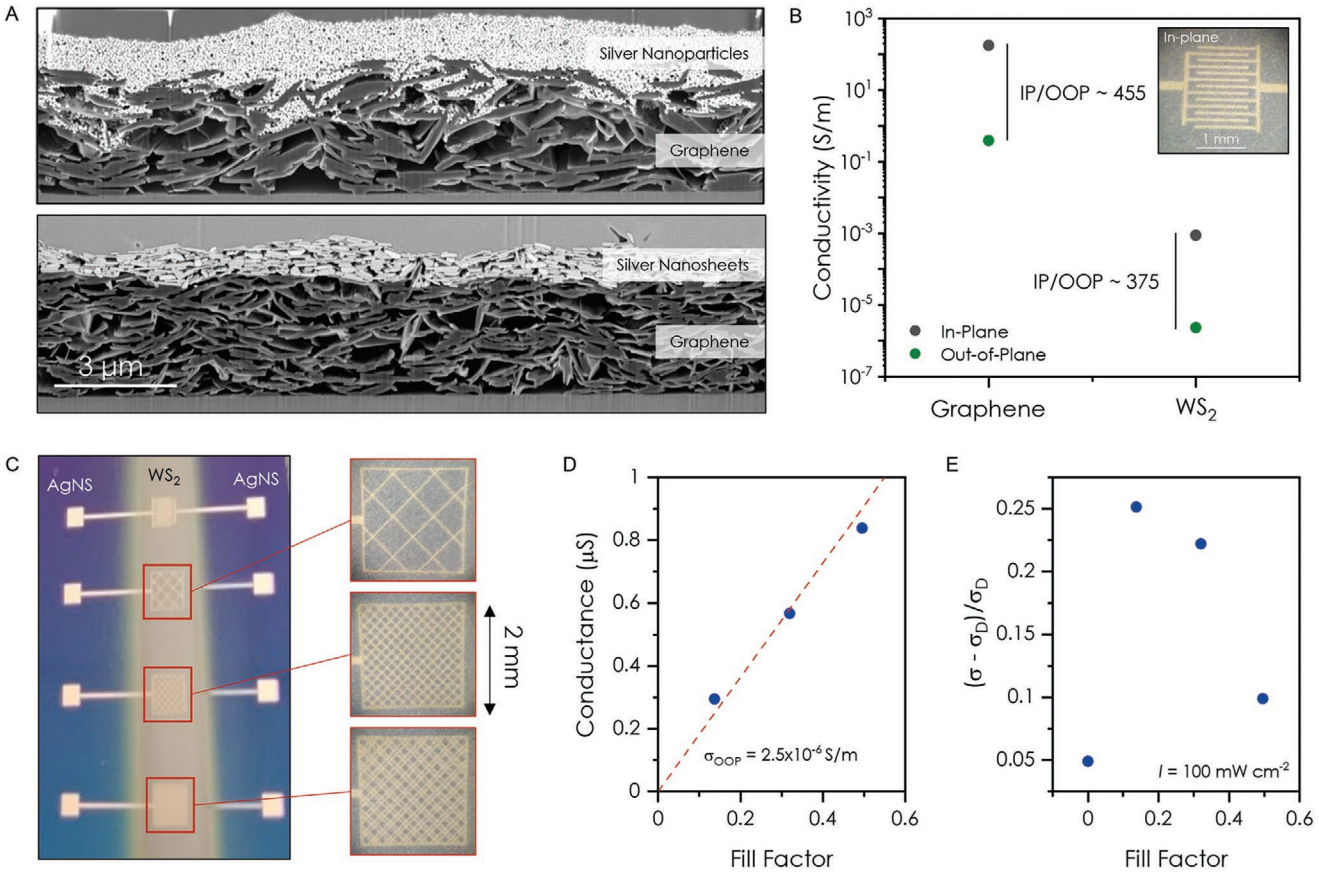

Figure 5. Aerosol-jet printed AgNS networks. A) FIB cross-sections of a spray-coated graphene network with an aerosol-jet printed top layer of AgNP (upper) and AgNS (lower). The AgNP can penetrate up to 1.5 µm into the graphene network where the AgNS form a smooth continuous interface. B) The in-plane (IP) and out-of-plane (OOP) conductivity of graphene and WS_2 networks measured using lateral and vertical structures with AgNS electrodes. C) A vertical heterostructure of AgNS/WS_2/AgNS where the AgNS are aerosol-jet printed and the WS_2 is spray coated. The bottom electrode is a 2 × 2 mm square while the top electrode is a mesh grid with sides of 2 × 2 mm and various pattern fills. D) The conductance of the heterostuctures in (C) against the fill factor of the top electrode. The fit is to Equation (2) which allows an OOP conductivity of 2.5×10^{-6} S m^{-1} to be extracted. E) The fractional increase in conductivity upon illumination, $(\sigma - \sigma_D)/\sigma_D$, where σ_D is the dark conductivity plotted against the fill factor of the top electrode. We see a large increase for low FF. An FF of zero indicates the measurement of the in-plane device.

better for deposition on glass, allowing annealing temperatures ≥200 °C and leading to conductivities of 1.5×10^7 S m^{-1}, ≈25% of bulk silver (see Supporting Information S16). This implies a value of $R_J = 1\ \Omega$ which is approaching the resistance of the nanosheets themselves (≈0.4 Ω). Furthermore, once the AgNS networks are annealed at 200 °C, they become extremely robust and cohesive, probably due to the formation of Ag filaments at junctions (see again Supporting Information S8).[41]

The conductivity of the annealed aerosol-jet printed networks also shows percolation-like scaling with thickness (Figure 4B) where a thickness-independent conductivity is reached at ≈150 nm for water-based (on PET, T_{anneal} = 100 °C) and C:T-based (on glass, T_{anneal} = 200 °C) inks, consistent with that of the TIJ networks. The AgNS networks deposited by the aerosol-jet printer also demonstrate a more uniform thickness distribution compared to the TIP as shown in Figure 4C (see also Supporting Information S17). The conductivity of the AJP networks is also constant with linewidth down to distances of 20 µm, suggesting very low line edge roughness (Figure 4B, inset). This is confirmed by measurements of the leakage conductance between parallel conducting traces (Figure 4D) which show electrical isolation for separations above 350 µm for the TIP but as low as 12 µm for the AJP (see Figure 4D, inset, and also Supporting Information S18 for a comparison of resolutions).

To further characterize the electrical properties of the AgNS networks, we measure the conductivity of an AJP network as a function of temperature shown in Figure 4E. The AgNS network shows metallic behavior down to 240 K (i.e., a positive temperature coefficient of resistivity) indicated by the dashed line. Below ≈180 K, we see a transition to a negative temperature coefficient of resistivity, behavior which has been observed in networks of AgNP,[49] $CoPt_3$ nanoparticles,[50] and PANI-sulfonic acid composites.[51] In the metallic region, the data is consistent with the Weidemann–Franz law, $\kappa/\sigma = L_{WF}T$, where κ is the thermal conductivity and L_{WF} is the Lorenz number. Taking $L_{WF} = 2.44 \times 10^{-8}$ W Ω K^{-2}[52] we estimate a room-temperature thermal conductivity of ≈91 W m^{-1} K^{-1}, or ≈21% of bulk silver, which demonstrates that heat conduction is also limited by inter-sheet junctions.

© 2022 The Authors. Small published by Wiley-VCH GmbH

Furthermore, comparing the AgNS network resistivity versus T data with that for an individual AgNW,[47] an AgNW network,[48] and bulk silver,[47] we clearly see the resistivity of the AgNS network is far lower than that of the AgNW network but is similar to that of an individual AgNW. This implies that the interface at the AgNS junctions may be more analogous to the internal AgNW grain boundaries than to interwire junctions.

The 2D-like aspect ratio of the AgNS is also important for integration into vertical heterostructures composed of porous materials. This is often very challenging due to the formation of shorts between top and bottom contacts.[53] **Figure 5**A (upper) shows a network of graphene nanosheets with a layer of AgNP printed on top. The small dimensions of the nanoparticles (d ≈50 nm) allow them to penetrate deep into the network up to distances of ≈1.5 µm. This is problematic as low temperature processing is usually achieved using nanoparticles with diameters less than 50 nm[54] or dissolved silver complexes.[24] In contrast, when the AgNS are deposited on a nanosheet network (Figure 5A, lower), their 2D-like geometry prevents them entering the voids which creates a distinct interface with the graphene network and precludes shorting (see also Supporting Information S19). This allows us to use the AgNS networks as electrodes to characterize both the in-plane (IP) and out-of-plane (OOP) conductivity of a given network. Figure 5B shows the resultant IP (see inset) and OOP conductivity of spray-coated networks of graphene and WS_2 using aerosol-jet printed AgNS electrodes (see Supporting Information S20 for nanosheet details). We find IP conductivities similar to previous reports for graphene[55] and WS_2[6,56] and OOP conductivities up to 455 times lower, consistent with the conductivity anisotropy seen across networks of layered materials.[57]

To demonstrate the utility of these vertical geometries, we print vertical heterostructures of AgNS/WS_2/AgNS as shown in Figure 5C where the bottom electrode is a 2 × 2 mm square and the top electrode is a 2 × 2 mm mesh grid with variable pattern fill, or fill factor, similar to those in Figure 3E. We see a linear variation in the OOP conductance with fill factor which can be fitted using

$$G_{\mathrm{OOP}} = \sigma_{\mathrm{OOP}} \frac{A}{t} FF \tag{2}$$

where t is the network thickness of 5.5 µm, A is the bottom electrode area of 4 mm^2, and FF is the fill factor of the top electrode. This allows a WS_2 OOP conductivity of 2.5×10^{-6} S m^{-1} to be extracted. We then place these structures under a solar simulator (100 mW cm^{-2}) and measure the fractional increase in conductivity, $(\sigma - \sigma_D)/\sigma_D$, as shown in the Figure 5E, where σ and σ_D are the illuminated and unilluminated conductivity, respectively. We see an increase in conductivity of ≈5% for the IP device (FF = 0). Interestingly, we see an increase in conductivity of ≈25% for the OOP heterostructures with the lowest FF, which then decreases with increasing FF. This compares with an in-plane fractional photoconductivity of ≈18% reported for inkjet-printed WS_2 networks.[58] We attribute this decrease in photoconductivity with increasing fill factor to the absorption of the AgNS in the UV–visible–NIR region (Supporting Information S12). This ability to photo-excite an active layer in a vertical heterostructure using a printed metal mesh electrode instead of a transparent conductor provides a new degree of flexibility in the design of optoelectronic devices.

3. Conclusions

We have shown that AgNS-based inks can be deposited into patterned thin films using printers of varying resolutions on both flexible and rigid substrates. Unannealed networks display conductivities up to 6 MS m^{-1}, rising to 15 MS m^{-1} after annealing at 200 °C. These high conductivities are due to very low junction resistances, which we associate with the 2D geometry of the nanosheets probably coupled with the formation of silver filaments within the junction region. However, it is worth noting that very little is known about the factors limiting network conduction, with the roles of network structure, interfaces, and oxidation particularly poorly understood. AgNS networks can be used in many applications, for example, extremely efficient EMI shields and printed electrodes. In the latter application, the 2D nature of the AgNS is critical for forming smooth short-free interfaces in vertical geometry devices.

Supporting Information

Supporting Information is available from the Wiley Online Library or from the author.

Acknowledgements

The authors acknowledge the European Commission (n° 696656, Graphene Flagship) and the European Research Council (FUTURE-PRINT). The authors have also received support from the Science Foundation Ireland (SFI)-funded centre AMBER (SFI/12/RC/2278_P2) and availed the facilities of the SFI-funded AML and ARL labs. T.C. acknowledges funding by a Marie Skłodowska-Curie Action "MOVE" (Grant Number 101030735, award number 16883, project number 211395).

Open access funding provided by IReL.

Conflict of Interest

The authors declare no conflict of interest.

Data Availability Statement

The data that support the findings of this study are available from the corresponding author upon reasonable request.

Keywords

electrodes, electromagnetic interference shielding, heterostructures, layered materials, printed electronics, silver nanosheets

Received: October 14, 2021
Revised: January 18, 2022
Published online:

© 2022 The Authors. Small published by Wiley-VCH GmbH

[1] A. G. Kelly, D. O'Suilleabhain, C. Gabbett, J. N. Coleman, *Nat. Rev. Mater.* **2021**, 1.
[2] F. Torrisi, T. Carey, *Nano Today* **2018**, *23*, 73.
[3] Z. Lin, Y. Huang, X. Duan, *Nature Electronics* **2019**, *2*, 378.
[4] a) A. Mazaheri, M. Lee, H. S. J. van der Zant, R. Frisenda, A. Castellanos-Gomez, *Nanoscale* **2020**, *12*, 19068; b) A. G. Kelly, C. Murphy, V. Vega-Mayoral, A. Harvey, A. S. Esmaeily, T. Hallam, D. McCloskey, J. N. Coleman, *2D Mater.* **2017**, *4*, 041006.
[5] a) B. Adilbekova, Y. Lin, E. Yengel, H. Faber, G. Harrison, Y. Firdaus, A. El-Labban, D. H. Anjum, V. Tung, T. D. Anthopoulos, *Journal of Materials Chemistry C* **2020**, *8*, 5259; b) M. Shanmugam, T. Bansal, C. A. Durcan, B. Yu, *Applied Physics Letters* **2012**, *100*, 153901.
[6] A. G. Kelly, T. Hallam, C. Backes, A. Harvey, A. S. Esmaeily, I. Godwin, J. Coelho, V. Nicolosi, J. Lauth, A. Kulkarni, S. Kinge, L. D. Siebbeles, G. S. Duesberg, J. N. Coleman, *Science* **2017**, *356*, 69.
[7] a) T. Carey, S. Cacovich, G. Divitini, J. Ren, A. Mansouri, J. M. Kim, C. Wang, C. Ducati, R. Sordan, F. Torrisi, *Nat. Commun.* **2017**, *8*, 1202; b) T. M. Higgins, S. Finn, M. Matthiesen, S. Grieger, K. Synnatschke, M. Brohmann, M. Rother, C. Backes, J. Zaumseil, *Adv. Funct. Mater.* **2018**, *29*, 1804387.
[8] a) K. Parvez, R. Worsley, A. Alieva, A. Felten, C. Casiraghi, *Carbon* **2019**, *149*, 213; b) S. Majee, M. Song, S. Zhang, Z. Zhang, *Carbon* **2016**, *102*, 51.
[9] a) R. A. Soots, E. A. Yakimchuk, N. A. Nebogatikova, I. A. Kotin, I. V. Antonova, *Tech. Phys. Lett.* **2016**, *42*, 438; b) F. Torrisi, T. Hasan, W. Wu, Z. Sun, A. Lombardo, T. S. Kulmala, G.-W. Hsieh, S. Jung, F. Bonaccorso, P. J. Paul, D. Chu, A. C. Ferrari, *ACS Nano* **2012**, *6*, 2992.
[10] M. Vural, A. Pena-Francesch, J. Bars-Pomes, H. Jung, H. Gudapati, C. B. Hatter, B. D. Allen, B. Anasori, I. T. Ozbolat, Y. Gogotsi, M. C. Demirel, *Adv. Funct. Mater.* **2018**, *28*, 1801972.
[11] C. J. Zhang, L. McKeon, M. P. Kremer, S. H. Park, O. Ronan, A. Seral-Ascaso, S. Barwich, C. O. Coileain, N. McEvoy, H. C. Nerl, B. Anasori, J. N. Coleman, Y. Gogotsi, V. Nicolosi, *Nat. Commun.* **2019**, *10*, 1795.
[12] C.-Y. Su, A.-Y. Lu, Y. Xu, F.-R. Chen, A. N. Khlobystov, L.-J. Li, *ACS Nano* **2011**, *5*, 2332.
[13] E. B. Secor, T. Z. Gao, A. E. Islam, R. Rao, S. G. Wallace, J. Zhu, K. W. Putz, B. Maruyama, M. C. Hersam, *Chem. Mater.* **2017**, *29*, 2332.
[14] a) X. J. Huang, T. Leng, X. Zhang, J. C. Chen, K. H. Chang, A. K. Geim, K. S. Novoselov, Z. R. Hu, *Appl. Phys. Lett.* **2015**, *106*, 203105; b) M. J. Large, S. P. Ogilvie, A. A. Graf, P. J. Lynch, M. A. O'Mara, T. Waters, I. Jurewicz, J. P. Salvage, A. B. Dalton, *Adv. Mater. Technol.* **2020**, *5*, 2000284.
[15] P. He, J. Cao, H. Ding, C. Liu, J. Neilson, Z. Li, I. A. Kinloch, B. Derby, *ACS Appl. Mater. Interfaces* **2019**, *11*, 32225.
[16] J. Zhang, N. Kong, S. Uzun, A. Levitt, S. Seyedin, P. A. Lynch, S. Qin, M. Han, W. Yang, J. Liu, X. Wang, Y. Gogotsi, J. M. Razal, *Adv. Mater.* **2020**, *32*, 2001093.
[17] J. L. Hart, K. Hantanasirisakul, A. C. Lang, B. Anasori, D. Pinto, Y. Pivak, J. T. van Omme, S. J. May, Y. Gogotsi, M. L. Taheri, *Nat. Commun.* **2019**, *10*, 522.
[18] H. Shi, C. Liu, Q. Jiang, J. Xu, *Adv. Electron. Mater.* **2015**, *1*, 1500017.
[19] L. Manjakkal, C. G. Nunez, W. T. Dang, R. Dahiya, *Nano Energy* **2018**, *51*, 604.
[20] S. De, J. N. Coleman, *ACS Nano* **2010**, *4*, 2713.
[21] T. Carey, C. Jones, F. Le Moal, D. Deganello, F. Torrisi, *ACS Appl. Mater. Interfaces* **2018**, *10*, 19948.
[22] a) A. Chiolerio, K. Rajan, I. Roppolo, A. Chiappone, S. Bocchini, D. Perrone, *Nanotechnol. Sci. Appl.* **2016**, *2016*, 1; b) A. Kamyshny, S. Magdassi, *Small* **2014**, *10*, 3515.
[23] a) Y.-L. Tai, Z.-G. Yang, *J. Mater. Chem.* **2011**, *21*, 5938; b) S. Jeong, H. C. Song, W. W. Lee, Y. Choi, B.-H. Ryu, *J. Appl. Phys.* **2010**, *108*, 102805.
[24] a) S.-P. Chen, Z.-K. Kao, J.-L. Lin, Y.-C. Liao, *ACS Appl. Mater. Interfaces* **2012**, *4*, 7064; b) Y. Mou, H. Cheng, H. Wang, Q. Sun, J. Liu, Y. Peng, M. Chen, *Appl. Surf. Sci.* **2019**, *475*, 75.
[25] H. Jiang, C. Tang, Y. Wang, L. Mao, Q. Sun, L. Zhang, H. Song, F. Huang, C. Zuo, *Appl. Surf. Sci.* **2021**, *564*, 150447.
[26] M. Vaseem, S.-K. Lee, J.-G. Kim, Y.-B. Hahn, *Chem. Eng. J.* **2016**, *306*, 796.
[27] S. B. Walker, J. A. Lewis, *J. Am. Chem. Soc.* **2012**, *134*, 1419.
[28] a) T. Kim, Y. W. Kim, H. S. Lee, H. Kim, W. S. Yang, K. S. Suh, *Adv. Funct. Mater.* **2013**, *23*, 1250; b) S. Lee, S. Shin, S. Lee, J. Seo, J. Lee, S. Son, H. J. Cho, H. Algadi, S. Al-Sayari, D. E. Kim, T. Lee, *Adv. Funct. Mater.* **2015**, *25*, 3114; c) D.-S. Leem, A. Edwards, M. Faist, J. Nelson, D. D. C. Bradley, J. C. de Mello, *Adv. Mater.* **2011**, *23*, 4371; d) F. S. F. Morgenstern, D. Kabra, S. Massip, T. J. K. Brenner, P. E. Lyons, J. N. Coleman, R. H. Friend, *Appl. Phys. Lett.* **2011**, *99*, 183307; e) T. Sannicolo, M. Lagrange, A. Cabos, C. Celle, J. P. Simonato, D. Bellet, *Small* **2016**, *12*, 6052.
[29] D. J. Finn, M. Lotya, J. N. Coleman, *ACS Appl. Mater. Interfaces* **2015**, *7*, 9254.
[30] a) S. Lu, J. A. Cardenas, R. Worsley, N. X. Williams, J. B. Andrews, C. Casiraghi, A. D. Franklin, *ACS Nano* **2019**, *13*, 11263; b) M. J. Donahue, A. Williamson, X. Strakosas, J. T. Friedlein, R. R. McLeod, H. Gleskova, G. G. Malliaras, *Adv. Mater.* **2018**, *30*, 1705031; c) P. Maisch, K. C. Tam, L. Lucera, H. J. Egelhaaf, H. Scheiber, E. Maier, C. J. Brabec, *Org. Electron.* **2016**, *38*, 139.
[31] a) T. Tokuno, M. Nogi, M. Karakawa, J. Jiu, T. T. Nge, Y. Aso, K. Suganuma, *Nano Res.* **2011**, *4*, 1215; b) E. C. Garnett, W. Cai, J. J. Cha, F. Mahmood, S. T. Connor, M. Greyson Christoforo, Y. Cui, M. D. McGehee, M. L. Brongersma, *Nat. Mater.* **2012**, *11*, 241; c) J. Jang, H.-G. Im, J. Jin, J. Lee, J.-Y. Lee, B.-S. Bae, *ACS Appl. Mater. Interfaces* **2016**, *8*, 27035.
[32] Y. Chao, H. Yang, Y. Li, S. Guo, C. Wang, C. Wang, *Chem. Phys. Lett.* **2018**, *708*, 183.
[33] H.-M. Ren, Y. Guo, S.-Y. Huang, K. Zhang, M. M. F. Yuen, X.-Z. Fu, S. Yu, R. Sun, C.-P. Wong, *ACS Appl. Mater. Interfaces* **2015**, *7*, 13685.
[34] a) Y.-I. Lee, S. Kim, S.-B. Jung, N. V. Myung, Y.-H. Choa, *ACS Appl. Mater. Interfaces* **2013**, *5*, 5908; b) Y.-L. Tai, Z.-G. Yang, *Surf. Interface Anal.* **2012**, *44*, 529.
[35] S. D. Hoath, *Fundamentals of Inkjet Printing: The Science of Inkjet and Droplets*, Wiley-VCH Verlag GmbH & Co. KgaA, Weinheim, Germany **2016**.
[36] M.-R. Azani, A. Hassanpour, T. Torres, *Adv. Energy Mater.* **2020**, *10*, 2002536.
[37] N. X. Williams, S. Noyce, J. A. Cardenas, M. Catenacci, B. J. Wiley, A. D. Franklin, *Nanoscale* **2019**, *11*, 14294.
[38] Z. Zhu, S.-Z. Guo, T. Hirdler, C. Eide, X. Fan, J. Tolar, M. C. McAlpine, *Adv. Mater.* **2018**, *30*, 1707495.
[39] Z. Lin, Y. Liu, U. Halim, M. Ding, Y. Liu, Y. Wang, C. Jia, P. Chen, X. Duan, C. Wang, F. Song, M. Li, C. Wan, Y. Huang, X. Duan, *Nature* **2018**, *562*, 254.
[40] a) A. T. Bellew, H. G. Manning, C. G. da Rocha, M. S. Ferreira, J. J. Boland, *ACS Nano* **2015**, *9*, 11422; b) F. Selzer, C. Floresca, D. Kneppe, L. Bormann, C. Sachse, N. Weiß, A. Eychmüller, A. Amassian, L. Müller-Meskamp, K. Leo, *Appl. Phys. Lett.* **2016**, *108*, 163302.
[41] T.-B. Song, Y. Chen, C.-H. Chung, Y. Yang, B. Bob, H.-S. Duan, G. Li, K.-N. Tu, Y. Huang, Y. Yang, *ACS Nano* **2014**, *8*, 2804.
[42] Y. Liu, W. Xiong, D. W. Li, Y. Lu, X. Huang, H. Liu, L. S. Fan, L. Jiang, J.-F. Silvain, Y. F. Lu, *Int. J. Extreme Manuf.* **2019**, *1*, 025001.
[43] D.-X. Yan, H. Pang, B. Li, R. Vajtai, L. Xu, P.-G. Ren, J.-H. Wang, Z.-M. Li, *Adv. Funct. Mater.* **2015**, *25*, 559.
[44] H. W. Ott, *Electromagnetic Compatibility Engineering*, John Wiley & Sons, Hoboken, NJ **2009**.
[45] a) K. T. Jacoby, M. W. Pieratt, J. I. Halman, K. A. Ramsey, in *Window and Dome Technologies and Materials* (Ed: R. W. Tustison), **2009**, 73020X; b) Y. Han, Y. Liu, L. Han, J. Lin, P. Jin, *Carbon* **2017**, *115*, 34.

© 2022 The Authors. Small published by Wiley-VCH GmbH

[46] a) A. Mahajan, C. D. Frisbie, L. F. Francis, *ACS Appl. Mater. Interfaces* **2013**, *5*, 4856; b) K. Hong, S. H. Kim, A. Mahajan, C. D. Frisbie, *ACS Appl. Mater. Interfaces* **2014**, *6*, 18704; c) M. Rother, M. Brohmann, S. Yang, S. B. Grimm, S. P. Schießl, A. Graf, J. Zaumseil, *Adv. Electron. Mater.* **2017**, *3*, 1700080.
[47] Z. Cheng, L. Liu, S. Xu, M. Lu, X. Wang, *Sci. Rep.* **2015**, *5*, 10718.
[48] Z. Cheng, M. Han, P. Yuan, S. Xu, B. A. Cola, X. Wang, *RSC Adv.* **2016**, *6*, 90674.
[49] a) R. C. Doty, H. Yu, C. K. Shih, B. A. Korgel, *J. Phys. Chem. B* **2001**, *105*, 8291; b) Sampaio, K. C. Beverly, J. R. Heath, *J. Phys. Chem. B* **2001**, *105*, 8797.
[50] A. J. Quinn, G. Redmond, *Prog. Solid State Chem.* **2005**, *33*, 263.
[51] M. Reghu, Y. Cao, D. Moses, A. J. Heeger, *Phys. Rev. B* **1993**, *47*, 1758.
[52] a) Y. Xiong, Y. Zhao, Y. Tao, F. Yao, D. Li, D. Xu, *Nano Lett.* **2020**, *20*, 8576; b) D. Kojda, R. Mitdank, M. Handwerg, A. Mogilatenko, M. Albrecht, Z. Wang, J. Ruhhammer, M. Kroener, P. Woias, S. F. Fischer, *Phys. Rev. B* **2015**, *91*, 024302.
[53] a) A. G. Kelly, D. Finn, A. Harvey, T. Hallam, J. N. Coleman, *Appl. Phys. Lett.* **2016**, *109*, 023107; b) Y. Nalawade, J. Pepper, A. Harvey, A. Griffin, D. Caffrey, A. G. Kelly, J. N. Coleman, *ACS Applied Electronic Materials* **2020**, *2*, 3233.
[54] a) M. Seo, J. S. Kim, J. G. Lee, S. B. Kim, S. M. Koo, *Thin Solid Films* **2016**, *616*, 366; b) D.-Y. Lee, Y.-S. Shin, S.-E. Park, T.-U. Yu, J. Hwang, *Appl. Phys. Lett.* **2007**, *90*, 081905; c) J. S. Kang, J. Ryu, H. S. Kim, H. T. Hahn, *J. Electron. Mater.* **2011**, *40*, 2268.
[55] a) K. Arapov, R. Abbel, G. de With, H. Friedrich, *Faraday Discuss.* **2014**, *173*, 323; b) M. Michel, C. Biswas, A. B. Kaul, *Appl. Mater. Today* **2017**, *6*, 16.
[56] D. O'Suilleabhain, V. Vega-Mayoral, A. G. Kelly, A. Harvey, J. N. Coleman, *ACS Appl. Mater. Interfaces* **2019**, *11*, 8545.
[57] a) G. Cunningham, M. Lotya, C. S. Cucinotta, S. Sanvito, S. D. Bergin, R. Menzel, M. S. Shaffer, J. N. Coleman, *ACS Nano* **2012**, *6*, 3468; b) G. Cunningham, U. Khan, C. Backes, D. Hanlon, D. McCloskey, J. F. Donegan, J. N. Coleman, *J. Mater. Chem. C* **2013**, *1*, 6899; c) X. Tian, M. E. Itkis, E. B. Bekyarova, R. C. Haddon, *Sci. Rep.* **2013**, *3*, 1710; d) S. Barwich, J. M. de Araujo, A. Rafferty, C. G. da Rocha, M. S. Ferreira, J. N. Coleman, *Carbon* **2021**, *171*, 306.
[58] D. McManus, A. Dal Santo, P. B. Selvasundaram, R. Krupke, A. LiBassi, C. Casiraghi, *Flex. Print. Electron.* **2018**, *3*, 034005.

© 2022 The Authors. Small published by Wiley-VCH GmbH